Performance of the Optical Communication Adaptive Optics Testbed

M. Troy,[1] J. Roberts,[1] S. Guiwits,[1] S. Azevedo,[1] S. Bikkannavar,[1] G. Brack,[1] V. Garkanian,[2]
D. Palmer,[1] B. Platt,[1] T. Truong,[1] K. Wallace,[1] and K. Wilson[2]

We describe the current performance of an adaptive optics testbed for optical communication. This adaptive optics system allows for simulation of nighttime and daytime observing on a 1-m telescope with a 97-actuator deformable mirror. In laboratory-generated seeing of 2.1 arcsec (at 0.5 μm), the system achieves a Strehl of 21 percent at 1.064 μm (210-nm rms wavefront). Predictions of the system's performance based on real-time wavefront sensor telemetry data and analytical equations are shown to agree with the observed image performance.

I. Introduction

The optical communication testbed is an adaptive optics (AO) system, designed and built at the Jet Propulsion Laboratory, that measures and corrects for simulated atmospheric turbulence in the path of an optical communications signal. The significance of measured improvements in the communications signal through the use of AO is dependent on a thorough understanding of AO system performance. Performance of an AO system can be characterized in many ways; in this article, we analyze the performance in terms of the mean-squared wavefront error (σ^2) which is a sum of individual, independent error terms (σ_i). In this analysis, error terms are decomposed into atmospheric fitting errors, temporal errors from the deformable and tip/tilt mirrors, and calibration errors. The AO telemetry system produced data for the performance analysis. A comparison of the predicted performance with the experimental results demonstrates good agreement.

The testbed description, given in Section II, includes information on the turbulence generator, deformable mirror, and optical path. Section III presents experimental results from open- and closed-loop AO system performance, along with a description of plate scale measurements. Section IV predicts the AO system performance considering spatial and temporal turbulence statistics, tip/tilt errors, high-order temporal errors, atmospheric errors, and calibration errors. We conclude this section with a comparison of predicted performance with experimental results.

---

[1] Interferometry and Advanced Optical Systems Section.

[2] Communications Architectures and Research Section.

The research described in this publication was carried out by the Jet Propulsion Laboratory, California Institute of Technology, under a contract with the National Aeronautics and Space Administration.

II. Testbed Description

The purpose of the testbed is to measure and correct for simulated atmospheric turbulence in the path of an optical communications signal. To this end, two wavelengths (1.064 μm and 635 nm) propagate through the system. One (635 nm) is used to measure and correct for the turbulence; the other (1.064 μm) is used to send data.

Figure 1 shows the optical layout of the AO system. Sources are injected via single mode fibers into collimating assemblies. The collimated beams are sent along the same path to the beam expander, which consists of an achromatic lens and an off-axis parabola (OAP). The expanded beam size was chosen to overfill the clear aperture of the deformable mirror.

The beams pass through a turbulence generator (see Fig. 2), which was custom designed and built at JPL to simulate the atmospheric conditions expected at the JPL Optical Communications Telescope Laboratory (OCTL) in Wrightwood, California, the ultimate location of the AO system. In the turbulence generator, four strip heaters are bolted to the bottom surface of an aluminum sheet. Another sheet of aluminum, perforated with 0.5-cm-diameter holes spaced on a 1-cm grid, is attached to the top of the sheet. The purpose of this top plate is to introduce uniform columns of heated air to the optical path.

The beams then reflect off the deformable mirror (DM). The DM, manufactured by Xinetics Corporation, consists of 97 actuators on a 7-mm grid spacing. The full diameter of the mirror contains 11 actuators. Each actuator has a stroke of 4 μm. The DM acts as the stop in the system and limits the beam size to 70 mm. The DM electronics were built by JPL and have a bandwidth of 5 kHz, significantly larger than the 2-kHz frame rate, so that no significant delay is created by the electronics.

The beam is compressed to 13.8 mm by optics identical to the expansion optics, which image the pupil (DM) onto the fast steering mirror (FSM). The FSM has a physical range of ± 1 mrad and provides tip/tilt correction.

The beam is then separated into its component wavelengths by a dichroic beam splitter (BS). The 635-nm light continues to the wavefront sensor (WFS). The WFS consists of a lenslet array, field-flattening

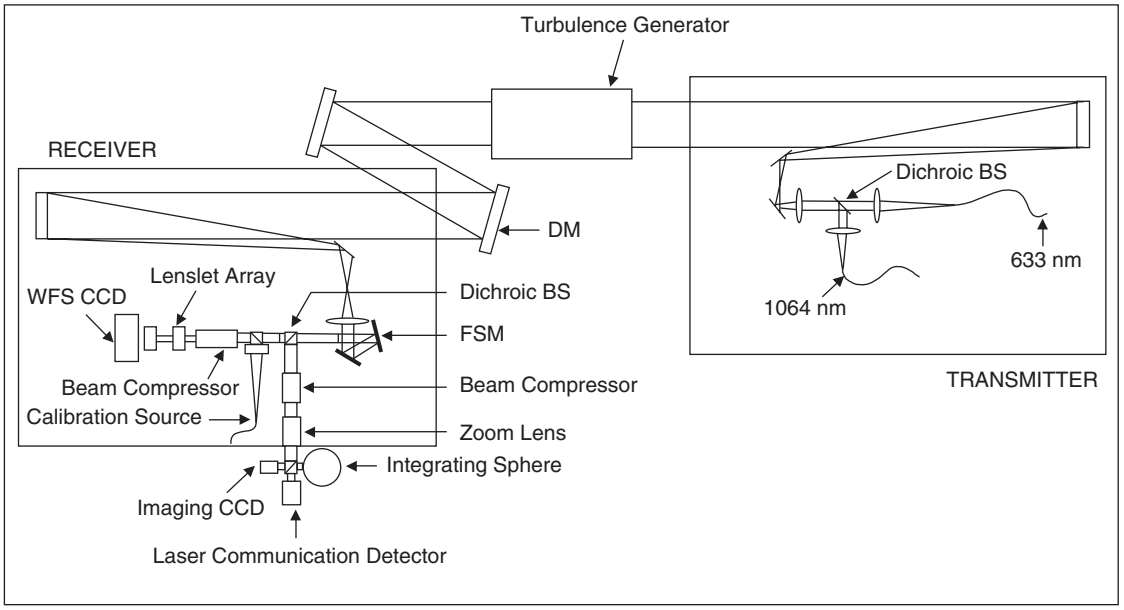

Fig. 1. Optical layout of the AO optical communication testbed.

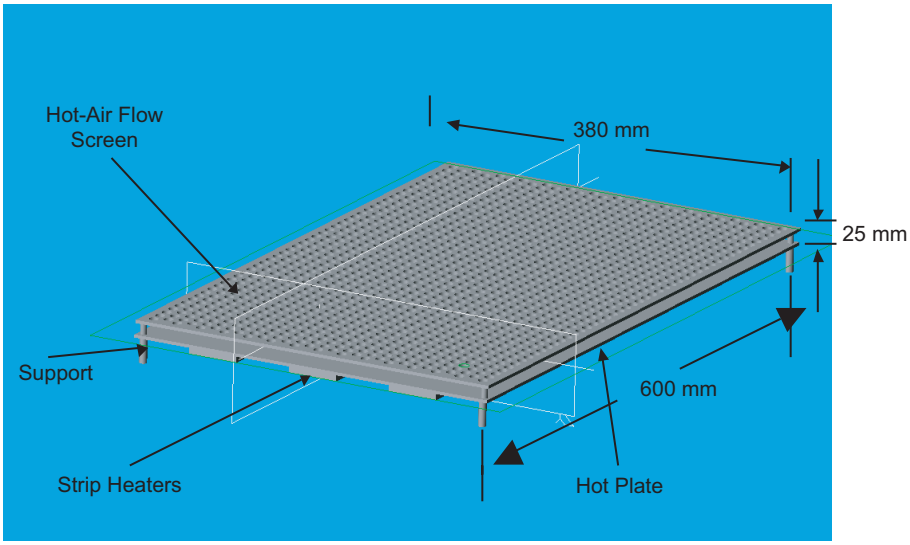

Fig. 2. Physical dimensions of the turbulence generator used in the testbed.

lens, relay lens, and the charge-coupled device (CCD) camera. A beam compressor images the DM onto the lenslet array and reduces the beam size to match the DM actuator spacing to the pitch of the lenslet array. The relay lens matches the grid of spots to the pixels of the CCD in order to implement quad cell centroiding. The CCD is an 80×80 pixel EEV39 [1]. We use only the center 40×40 pixels, which are binned on chip down to 20×20 (2×2 pixels per subaperture). The camera runs at speeds up to 2.1 kHz with a read noise of 6.4 electrons per pixel. When slowed below 450 Hz, read noise drops to 3.7 electrons per pixel.

Along the communications path, the 1.064-μm beam is reduced further and focused onto the detector using a zoom lens. The zoom lens allows simulation of different detector sizes by changing the size of the focused spot. A portion of the light is split off to an imaging CCD. This allows monitoring of the beam quality and AO system performance. An integrating sphere injects background noise into the signal to simulate different background noise conditions.

Elements along the communications path are not measured by the WFS, preventing wavefront error correction. Similarly, wavefront errors in the WFS path are measured and corrected, but that correction may increase wavefront error along the communications path. These are the non-common path errors. Since the goal is to improve the optical quality along the communications path, these static wavefront errors must be calibrated out to give the best spot on the imaging camera. See Section IV.D for further discussion of these error terms.

The control software, user interface, and computer systems are a modified copy of the versions used on the Palomar AO system [2]. This system takes the pixel data from the WFS, calculates centroids, reconstructs the wavefront (via a matrix multiply with a reconstructor matrix), and implements a servo loop before sending commands to the DM and FSM. The real-time system can run at up to 2,000 frames per second. With a 2-kHz frame rate, we expect a closed-loop bandwidth of about 80 Hz, the same values achieved on a similar AO system at the Palomar Hale telescope. In addition, the computer system can record real-time telemetry data at rates up to 400 Hz. The 400-Hz telemetry rate is important in order to allow analysis of the AO system performance. These data include the centroid position, centroid flux, reconstructed wavefront, DM actuator positions, and FSM positions.

III. Experimental Results

A. Results

For all experimental data presented here, the AO system used a reconstructor generated with the software package A++ and ran at a frame rate of 2000 Hz. Image data were collected using the imaging CCD on the communications path (1.064 μm). Each image is the background subtracted average of 200 frames, giving an approximate integration time of 15 s. Data were first taken under nominal laboratory conditions to establish the baseline wavefront error. The turbulence generator then was set to 230 deg C, and the temperature was allowed to stabilize. The resulting open- and closed-loop images are shown in Fig. 3, plotted on a log scale. Bit-error-rate data for the communications signal were collected concurrently, as described in [3].

The Strehl ratio (the ratio of peak intensities in the aberrated and ideal point spread functions) is used to determine the improvement in beam quality produced by the AO system. To calculate the Strehl ratio, diffraction-limited Airy images were generated using the plate scale (see Section III.B) for each specific zoom setting and the calculated center of the measured spot. These were compared to the normalized image data to obtain the Strehl ratio.

Data were collected at different zoom settings for both nominal and turbulated conditions. Figure 4 shows measured Strehl ratios converted to wavefront error using the Marechal [4] approximation $S = e^{-(2\pi(\mathrm{WFE}/\lambda))^2} = e^{-\sigma^2}$. Baseline data for zoom setting 2 were removed due to saturation in the images. The residual wavefront error associated with the AO correction is just the increase in wavefront error between the closed loop with turbulence wavefront error (cl_wfe) and the wavefront error without turbulence (static_wfe). We call this the relative AO system performance; it is calculated by taking the quadrature difference, which is $\sqrt{cl\_wfe^2 - \mathrm{static}\_wfe^2}$. The graph shows that the AO system corrects all but about 100 nm of the turbulence-induced WFE. These measurements were performed before a manual calibration of the system, as described in Section IV.D. The manual calibration points shown on the graph represent the optimal baseline WFE of the system.

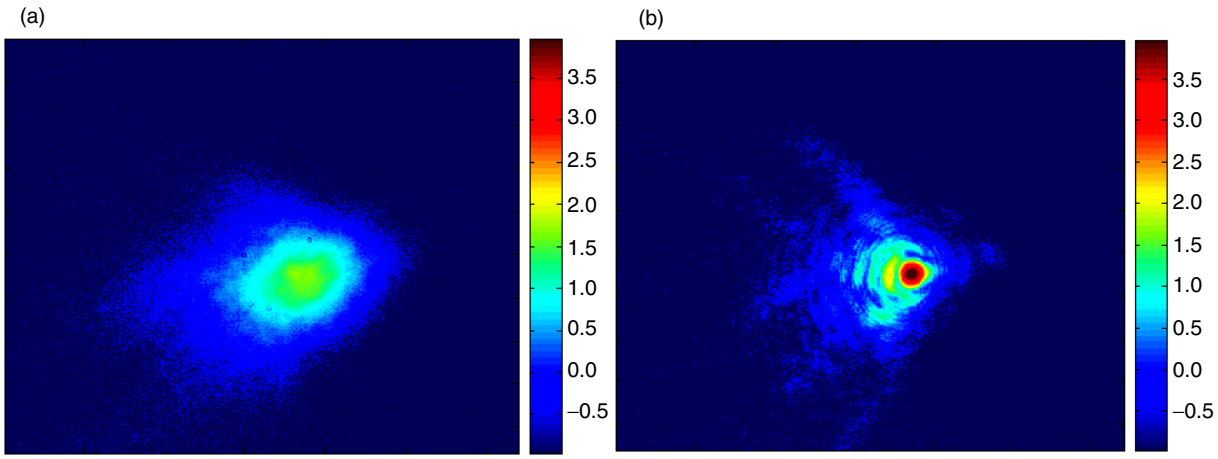

Fig. 3. Images with the turbulence generator turned on: (a) open loop and (b) closed loop. The open-loop image has a FWHM of 1428 μm **or** 5.8 λ/*D*. **The closed-loop image has a FWHM of** 246 μm **or** 1 λ/*D*. **Data were taken at a zoom of 4.**

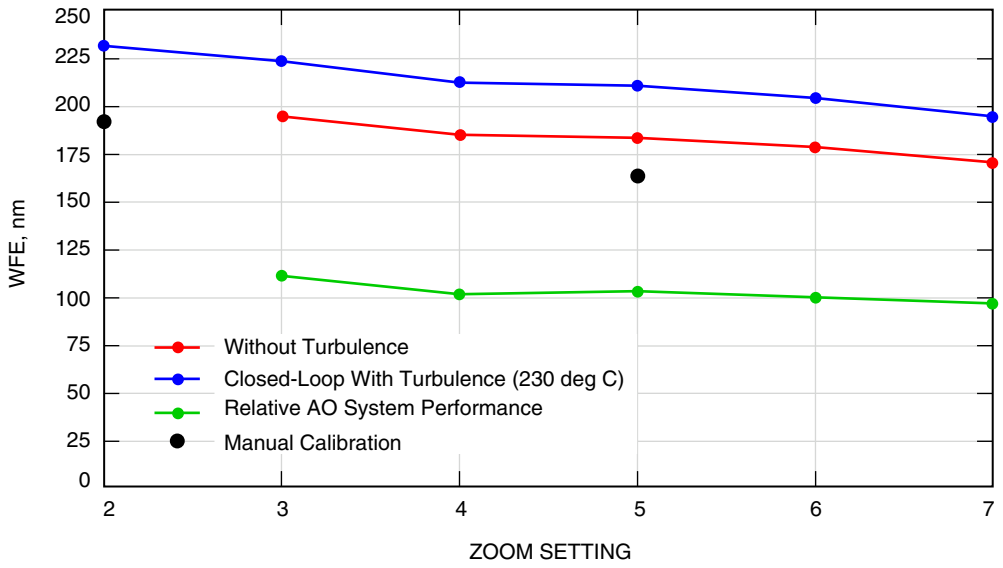

Fig. 4. The rms wavefront error versus zoom setting with the turbulence generator turned on and off. Also plotted is the relative AO system performance, which is defined as the subtraction (in quadrature) of the turbulence on and off results.

B. System Plate Scale Measurements

The plate scale of the system gives the relationship between the angle of tilt in the incoming beam and the spot movement at the detector. For the purpose of determining plate scale, the system acts as if the 70-mm beam travels through a single powered element with a system focal length (SFL) that preserves the final F/# of the system. Therefore, the plate scale is Δtilt angle/Δspot position = 1/SFL. The SFL is determined by the output focal length and the total magnification in the system (shown in Fig. 5). In our system, the SFL = (5.08 $*$ 5 $*$ zoom magnification) $*$ 164 mm or more simply 4165.6 mm $*$ zoom magnification.

As a check on these calculations, Airy images were generated using the calculated plate scale for each zoom setting. If the calculated plate scale were correct, the Airy rings would be located at the same place in the theoretical and measured images, although aberrations in the real system will make the rings less distinct. A scaling error appeared when theoretical images were compared with data taken at each zoom setting (Fig. 6). By adjusting the plate scales used to generate the Airy images, the Airy pattern in the generated data was matched to the pattern in the measured data. It was determined that the required adjustments gave an average difference of 8 percent in the plate scale.

This discrepancy could be due to a cumulative effect of slight variations in the focal length or magnification of the zoom lens and magnification of the beam compressor. Based on these results, the measured plate scales (Table 1) are used for all subsequent calculations, including Strehl ratio and r_0.

IV. Analysis of AO System Performance

The performance of an AO system can be characterized in many ways; in this section, we analyze the performance in terms of the mean-squared wavefront error (σ^2), which is a sum of individual error terms (σ_i). Data from the AO telemetry system (as described in Section II) are used in the following analysis. Although the camera frame rate is 2000 Hz, every 20th frame was recorded (although the system is capable of recording every 5th frame), reducing the effective frequency of the telemetry data to 100 Hz.

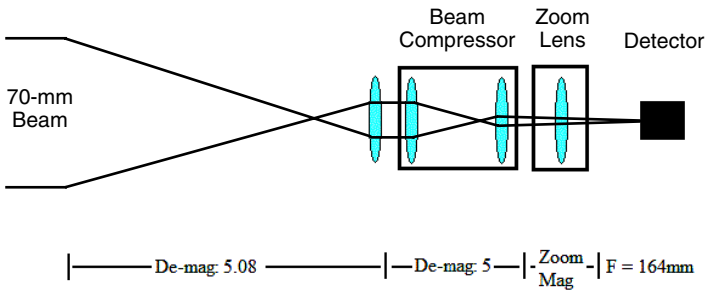

Fig. 5. Simplified layout of the 1.064 μm **optical path.**

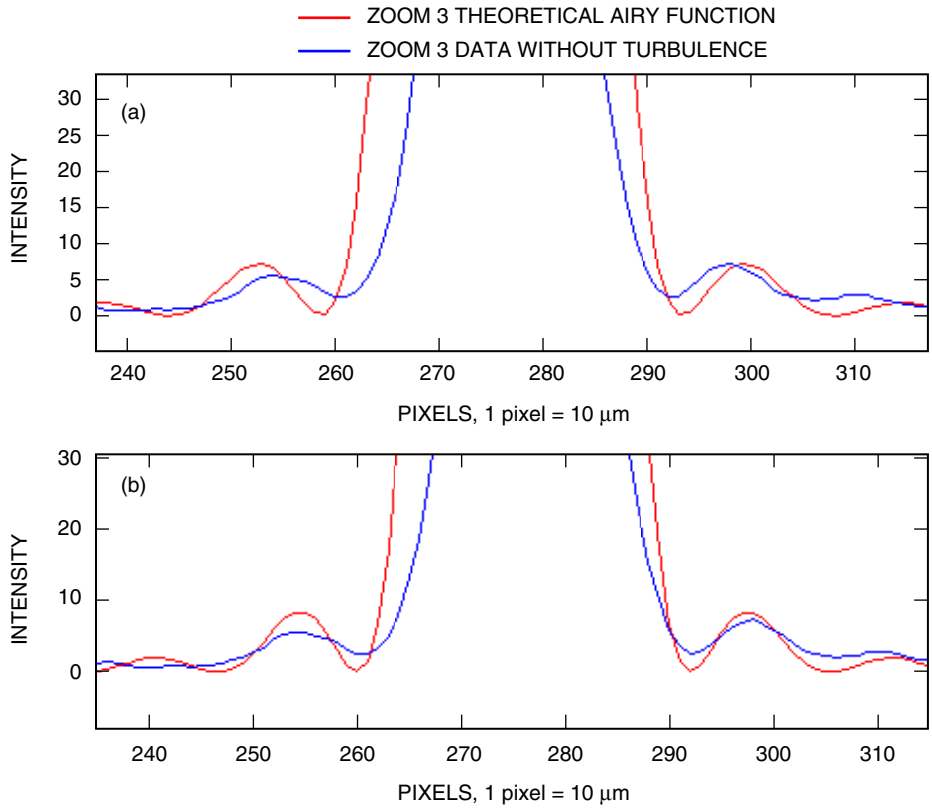

Fig. 6. Comparison of measured data with the generated Airy image: (a) Airy image generated using theoretical plate scale and (b) Airy image generated using adjusted plate scale. The plate scale was adjusted by 8 percent so that the zeros of the Airy function agreed with the measured data. The wavelength is 1064 μm.

In Section IV.A, we analyze the turbulence statistics provided by the turbulence generator described in Section II. In Sections IV.B through IV.D, we decompose error terms into temporal errors, calibration errors, and atmospheric fitting error terms arising from the inability to correct spatial frequencies smaller than the actuator spacing. The signal in the wavefront sensor was large compared with the CCD read noise, allowing us to ignore measurement error in the analysis. In Section IV.E, we bring all the error terms together and compare the predicted performance with the experimental results from Section III.

Table 1. Calculated plate scales.

Zoom setting	Real magnification	Analytical SFL, mm	Analytical plate scale, arcsec/mm (70-mm beam)	Measured plate scale, arcsec/mm (70-mm beam)
1	0.75	3,124.20	66.02	71.42
2	1.5	6,248.40	33.01	35.71
3	2.25	9,372.60	22.01	23.80
4	3	12,496.80	16.51	17.85
5	3.75	15,621.00	13.20	14.28
6	4.5	18,745.20	11.00	11.90
7	5.25	21,869.40	9.43	10.20

A. Turbulence Statistics

Atmospheric turbulence has both spatial and temporal characteristics. As will be shown below, both of these characteristics significantly impact the performance of the AO system, although all too often only the spatial characteristics are considered.

1. Spatial Characteristics. The atmospheric coherence length (referred to as the Fried parameter [5]) can be used to describe the spatial characteristics of the turbulence. The Fried parameter, denoted as r_0, is the diameter of a circle that encloses 1 radian-squared of wavefront error. Equivalently, an uncompensated long-exposure image will have an angular full-width half-maximum (FWHM) of $\theta = \lambda/r_0$: the observing wavelength divided by r_0. The Fried parameter is usually quoted at 0.5 μm unless stated otherwise and depends on wavelength as $\lambda^{6/5}$. From the open-loop image (Section III.A), an r_0 in the 70-mm beam of 8.6 mm at 1.064 μm is estimated. The optical communication testbed simulates the performance on a 1-m telescope. So, the r_0 for a 1-m telescope would be 12.3 cm (at 1.064 μm) or 5.0 cm (at 0.5 μm). This is equivalent to 2.1 arcsec seeing—fairly poor conditions for astronomical sites at night, but typical for daytime observations at the OCTL [6].

2. Temporal Characteristics. The rate at which the AO system needs to measure and correct the wavefront is dictated by the speed at which atmospheric turbulence changes. One way to characterize the temporal characteristics is to measure the turbulence-weighted wind velocity (v). Figure 7 shows a plot of the open-loop tip/tilt power spectral density (PSD), calculated from the wavefront sensor telemetry with AO control loops turned off. Atmospheric theory predicts that a change in slope should occur at v/D (D is the diameter of the telescope, 1 m in this analysis—not the size of the beam in the testbed). Figure 7 shows a change in slope at 1 Hz, implying a wind velocity of $\sim$1 m/s. This result reveals a limitation in the turbulence generator, since mean wind velocities during operation are 10–15 m/s at astronomical sites [7, pp. 87–88]. In order to increase the wind velocity generated in the testbed, fans have been added to the turbulence generator, and turbulence statistics will be retested in the future.

B. Temporal Errors

The finite time required to measure the atmospheric wavefront and apply the correction to the appropriate control device (deformable or fast-steering mirror) contributes to the residual wavefront error in the AO system. Below we calculate the theoretical values for both tip/tilt and high-order (all modes besides tip/tilt) corrections.

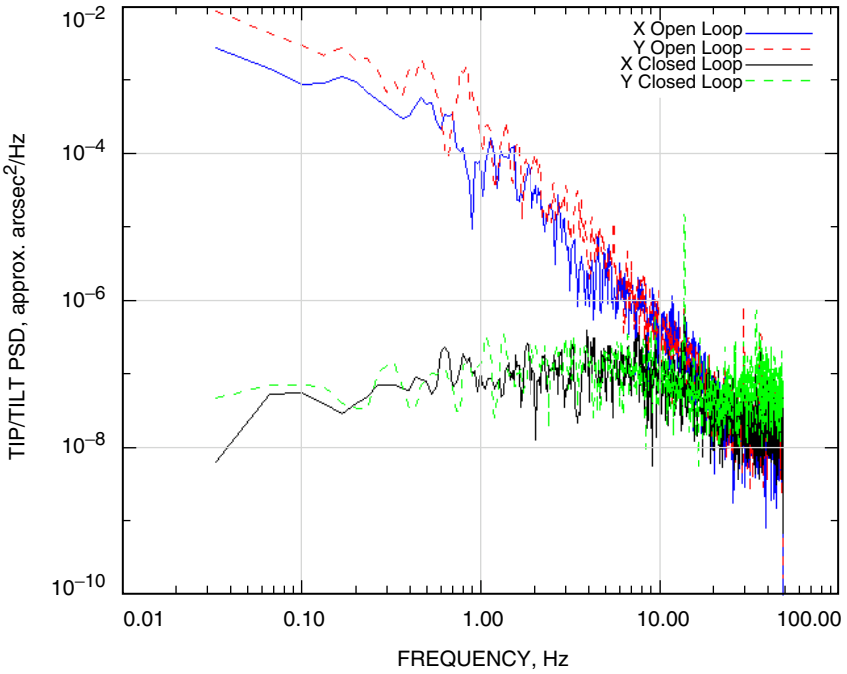

Fig. 7. The open- and closed-loop tip/tilt PSD with the turbulence generator turned on. The servo bandwidth is estimated to be about 10 Hz, **and the wind velocity is** ~1 m/s.

1. Tip/Tilt Temporal Errors. The two-axis residual tip/tilt error (in radians) from the finite bandwidth of an AO system is given by [8]

$$\sigma_{\text{Temporal\_TT}} = \sqrt{2}\left(\frac{f_t}{f_{3\text{dB}}}\right)\left(\frac{\lambda}{D}\right)\text{[rad]} \tag{1}$$

where $f_{3\text{dB}}$ is the -3 dB point of the servo bandwidth and f_t is the fundamental tracking frequency, which can be approximated by

$$f_t = 0.0811\left(\frac{r_0}{D}\right)^{1/6}\left(\frac{v}{r_0}\right)\text{[Hz]} \tag{2}$$

The servo bandwidth (Fig. 7) is ∼10 Hz—approximately 10 times lower than the expected servo bandwidth. A typical servo bandwidth is 20 times lower than the wavefront sensor frame rate. This would correspond to ∼100 Hz for our 2000-Hz frame rate. We believe that the lower than expected values are due to non-optimal servo control parameters. However, the wind velocity generated in the turbulator was also approximately a factor of 10 lower than the expected value in the field (Section IV.A.2), resulting in a tracking frequency 10 times lower than expected in the field. Thus, in the calculation of tip/tilt temporal errors, the lower than expected tracking frequency cancels out the lower than expected servo bandwidths. Therefore, these results are typical of what we should achieve on the sky after optimization of the AO servo bandwidths. Using $r_0 = 5.0$ cm (from Section IV.A.1), a wind velocity of 1 m/s, a D of 1 m, and a wavelength of 0.5 μm results in a tracking frequency of 0.99 Hz and a residual tip/tilt error of 0.0145 arcsec. This is $0.07\lambda/D$, or 25 nm of wavefront error.

2. High-Order Temporal Errors. The rms phase error (in radians) resulting from the finite control bandwidth of the deformable mirror is given by [7, pp. 337–338]

$$\sigma_{\text{Temporal\_DM}} = \left(\frac{f_g}{f_{3\text{dB}}}\right)^{5/6} \text{[rad]} \tag{3}$$

where f_g, the Greenwood frequency, is given by

$$f_g = \left(\frac{0.427v}{r_0}\right) \text{[Hz]} \tag{4}$$

Figure 8 shows the open- and closed-loop reconstructed phase errors. The PSD is calculated for each subaperture and averaged over all subapertures. Data for the PSD come from running the AO system with the DM loops open and closed and recording telemetry at 100 Hz. The estimated servo control bandwidth is 10 Hz. As has been noted in the previous section, this value is approximately 10 times lower than the expected value, and is most likely due to non-optimal servo control parameters. As in Section IV.B.1, this is offset by the lower wind velocity in the testbed. The calculated Greenwood frequency is 8.58 Hz, which results in 70 nm of wavefront error.

C. Atmospheric Fitting Errors

The atmospheric fitting error refers to the inability of the AO system to correct wavefront errors on spatial scales smaller than approximately $2 * d$, where d is the spacing between actuators at the primary mirror (10 cm in our testbed, which simulates a 1-m telescope). The fitting error from a continuous face sheet DM is given by [7, pp. 342–343]

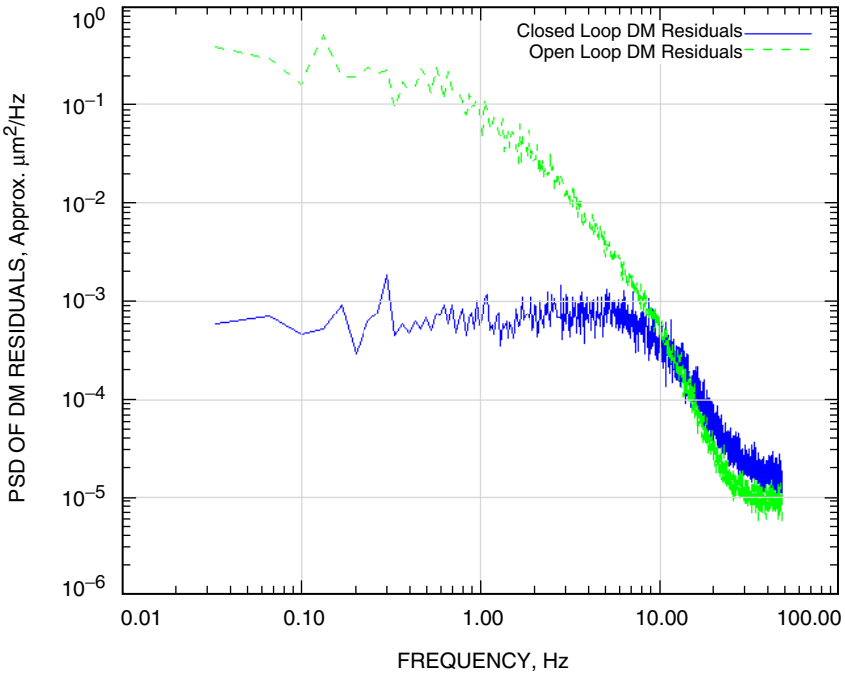

Fig. 8. The PSD of the open- and closed-loop DM residuals with the turbulence generator on. The PSDs were calculated for each DM actuator and averaged. The servo bandwidth is about 10 Hz**.**

$$\sigma_{\text{Atm\_Fitting}} = 0.49 \left(\frac{d}{r_0} \right)^{5/6} \text{[rad]} \tag{5}$$

This results in an error of 70 nm given the measured r_0 value of 5.0 cm.

D. Calibration

The Shack–Hartmann wavefront sensor detects aberrations in the optical path of the sensing 635-nm wavelength but does not measure wavefront errors in the non-common optical path of the communications system. Correspondingly, any aberrations in the WFS are non-common path and degrade the quality of the wavefront in the communications path. In order to optimize the performance of the AO system, these errors need to be taken into account. Hence, rather than driving the Shack–Hartmann images of the beacon on the 10×10 subapertures to the centers of the corresponding 2×2 quad cells, centroids are driven to an offset value to produce an optimized wavefront in the communications path.

The first step in the calibration is to determine the DM shape that maximizes Strehl in the communications path. An application was written that allowed arbitrary Zernike [7, pp. 95–96] modes to be applied to the DM. Beginning with the low-order terms, each Zernike mode is adjusted individually to optimize Strehl before continuing to the next mode. The first three Zernike modes (piston, tip, and tilt) remain zero, since piston does not change the shape of the DM, and the tip/tilt correction is done using the steering mirror, rather than the DM. Once the optimal coefficient is determined, the process continues with the next Zernike mode. The first 15 Zernike modes were examined using this method. After the optimal DM shape is determined, the centroid values in the WFS are recorded and used as the desired centroid values in the future.

Our results indicate that the wavefront error in the communications path is a function of the zoom (see the without-turbulence data in Fig. 4). We used the above method to determine the first 15 Zernike coefficients at a zoom setting of 5. Before calibration, the imaging camera routinely measured ∼39 percent Strehl. After applying the above correction to the DM, the AO system consistently achieved Strehl ratios of 47 percent or higher. The same procedure was used at a zoom setting of 2, but no significant improvement could be made from the optimal settings determined for a zoom of 5. The optimal DM shape produced a Strehl of 28 percent. One theory is that changing the zoom lens introduces wavefront aberrations. In this case, one would expect these to be low-order aberrations that could be tuned out using the above procedure. However, even after calibration, the Strehl from the zooms of 2 and 5 are significantly different, suggesting that the problem is due to a cause other than wavefront aberrations introduced from changing the zoom. The difference in wavefront error as a function of zoom may be due to scattered light (see Fig. 3) or another related optical alignment problem. We plan to investigate this in the future.

E. Comparison of Predicted Performance to Experimental Results

Error terms calculated in the above section are added in quadrature and displayed in Table 2. The total predicted wavefront error of 210 nm appears to match the measured value (Section III.A) of 210 nm. However, this is not a very strong test as the dominant error term is the calibration error (184 nm), which is always a measured value. Ignoring the calibration error, the predicted rms wavefront error is 102 nm as compared with the measured value (Section III.A) of 102 nm. These values are in very good agreement. The current system is limited by both atmospheric fitting error and temporal delay in updating the DM. Assuming we increase the system bandwidth to the predicted values (approximately 10 times better) and that the atmospheric wind velocities are of the order 10–15 m/s (versus the 1 m/s in the experiment), the DM temporal error will not change and the system on the sky will continue to be dominated by these two error terms.

Table 2. Predicted and measured AO system performance. The predicted wavefront error of 102 nm agrees very well with the measured value of 102 nm. There is an additional 184 nm of calibration error, which was only determined experimentally.

Error term	Predicted rms wavefront error, nm	Measured rms wavefront error, nm
Atmospheric fitting	70	NA
DM temporal	70	NA
Tip/tilt temporal	25	NA
Subtotal error	102	102
Calibration (zoom = 5)	184	⟸184
Total error	210	210

V. Conclusions and Future Work

We have designed and built an adaptive optics testbed for optical communication, and have shown that the measured performance of the system agrees with the theoretical performance predicted by analytical equations. Furthermore, the system performance is limited by calibration of the non-common path. Excluding calibration errors, the system achieves 102-nm rms of wavefront error. This increases to 210 nm when calibration errors are included.

In the future, we plan to improve the turbulence generator to simulate correctly the magnitude of wind velocity expected from the atmosphere. We also will optimize the servo loops to obtain a higher closed-loop bandwidth. There are also plans to investigate and correct the suspected scattered light in the imaging path. In order to better understand the system performance, we plan to calibrate the WFS, FSM, and reconstructor. This will enable direct measurement of the tip/tilt bandwidth, DM bandwidth, and WFS measurement errors from telemetry data. These values then can be compared with the analytical values to better understand and validate the system performance.

References

[1] R. DuVarney, C. Bleau, G. Motter, S. Shaklan, A. Kunhnert, G. Brack, D. Palmer, M. Troy, T. Kieu, and R. Dekany, "EEV CCD39 Wavefront Sensor Cameras for AO and Interferometry," in *Advanced Optical Systems Technology*, P. Wizinowich, ed., Proc. SPIE 4007, pp. 481–492, 2000.

[2] T. Truong, G. Brack, M. Troy, T. Trinh, F. Shi, and R. Dekany, "Real-Time Wavefront Processor for the Next Generation of Adaptive Optics Systems: A Design and Analysis," in *Adaptive Optical System Technologies II*, P. Wizinowich and D. Bonaccini, eds., Proc. SPIE 4839, pp. 911–922, 2003.

[3] M. W. Wright, M. Srinivasan, and K. Wilson, "Improved Optical Communications Performance Using Adaptive Optics with an Avalanche Photodiode Detector," *The Interplanetary Network Progress Report*, vol. 42-161, Jet Propulsion Laboratory, Pasadena, California, pp. 1–13, May 15, 2005.
http://ipnpr/progress_report/42-161/161D.pdf

[4] V. Mahajan, "Strehl Ratio or Primary Aberrations: Some Analytic Results for Circular and Annular Pupils," *J. Opt. Soc. Am.*, vol. 71, pp. 1258–1266, 1982.

[5] D. Fried, "Optical Resolution Through a Randomly Inhomogeneous Medium for Very Long and Very Short Exposures," *J. Opt. Soc. Am.*, vol. 56, pp. 1372–1379, 1966.

[6] K. Wilson, A. Vaughan, J. Wu, D. Mayes, J. Maloney, and R. Sobek, "Preliminary Characterization Results of the Optical Communications Telescope Laboratory Telescope," *The Interplanetary Network Progress Report*, vol. 42-161, Jet Propulsion Laboratory, Pasadena, California, pp. 1–14, May 15, 2005. http://ipnpr/progress_report/42-161/161M.pdf

[7] J. Hardy, *Adaptive Optics for Astronomical Telescopes*, 1st. ed., New York: Oxford University Press, 1998.

[8] G. Tyler, "Bandwidth Considerations for Tracking Through Turbulence," *J. Opt. Soc. Am.*, vol. 11, pp. 358–367, 1994.